



Cite this: *Nanoscale*, 2017, **9**, 17722

Received 9th September 2017,
 Accepted 6th November 2017

DOI: 10.1039/c7nr06721f

rsc.li/nanoscale

2D molybdenum and vanadium nitrides synthesized by ammoniation of 2D transition metal carbides (MXenes)[†]

Patrick Urbankowski,^a Babak Anasori,^a Kanit Hantanasirisakul,^a Long Yang,^b Lihua Zhang,^c Bernard Haines,^a Steven J. May,^a Simon J. L. Billinge^{b,d} and Yury Gogotsi^{b,*a}

MXenes are a rapidly growing class of 2D transition metal carbides and nitrides, finding applications in fields ranging from energy storage to electromagnetic interference shielding and transparent conductive coatings. However, while more than 20 carbide MXenes have already been synthesized, Ti₄N₃ and Ti₂N are the only nitride MXenes reported so far. Here by ammoniation of Mo₂CT_x and V₂CT_x MXenes at 600 °C, we report on their transformation to 2D metal nitrides. Carbon atoms in the precursor MXenes are replaced with N atoms, resulting from the decomposition of ammonia molecules. The crystal structures of the resulting Mo₂N and V₂N were determined with transmission electron microscopy and X-ray pair distribution function analysis. Our results indicate that Mo₂N retains the MXene structure and V₂C transforms to a mixed layered structure of trigonal V₂N and cubic VN. Temperature-dependent resistivity measurements of the nitrides reveal that they exhibit metallic conductivity, as opposed to semiconductor-like behavior of their parent carbides. As important, room-temperature electrical conductivity values of Mo₂N and V₂N are three and one order of magnitude larger than those of the Mo₂CT_x and V₂CT_x precursors, respectively. This study shows how gas treatment synthesis such as ammoniation can transform carbide MXenes into 2D nitrides with higher electrical conductivities and metallic behavior, opening a new avenue in 2D materials synthesis.

Introduction

MXenes, a family of two-dimensional (2D) transition metal carbides, carbonitrides and nitrides, have attracted much attention for their excellent properties and applications, and research is continuing to grow.^{1–5} These properties, including their hydrophilic surfaces and high electrical conductivities,^{1,6,7} make them promising in energy storage devices,^{6–9} electromagnetic interference (EMI) shielding,^{10,11} and many other applications.^{12–21} Carbide MXenes have been most commonly produced by selectively etching out the A-element layer from a MXene's corresponding ternary carbide precursor (usually a MAX phase) in hydrofluoric acid (HF).¹ The term MAX phase is derived from its constituent elements in the general formula M_{n+1}AX_n, where M is an early transition metal, A is a group IIIA or IVA element, X is C and/or N, and *n* = 1, 2 or 3.² For example, when Ti₃AlC₂ is treated in HF, Al is selectively etched and this process yields the MXene Ti₃C₂T_x, where T_x represents the terminating groups along the two faces of each 2D flake such as –F, –O, and –OH.²

Nitride MXenes have attracted attention for their potential applications in energy storage and plasmonics^{22,23} due to their higher electrical conductivities,²⁴ which are expected to be higher than those of carbide MXenes.²⁵ For example, 2D MoN films have been shown to exhibit a very high volumetric capacitance of 928 F cm^{–3} in sulfuric acid electrolyte and excellent rate performance.²⁶ MXenes theoretically include the same number of nitrides and carbides.²⁷ Since attempts to synthesize nitride MXenes *via* methods used for carbide MXenes have failed, however, it was not until recently when the first nitride MXene (titanium nitride, Ti₄N₃) was synthesized with a novel molten salt etching synthesis approach,^{28,29} followed by the synthesis of Ti₂N.²³ Lack of focus on finding high-yield synthesis methods have prevented not only MXene nitrides, but 2D nitrides in general, and their applications from developing further. Only a few 2D nitrides including MoN,²⁶ GaN,³⁰ Ti₄N₃,²⁸ and Ti₂N²³ have been reported so far. Current strategies for synthesis of 2D nitrides are mostly limited to

^aA.J. Drexel Nanomaterials Institute and Department of Materials Science & Engineering, Drexel University, Philadelphia, PA 19104, USA.

E-mail: gogotsi@drexel.edu; Fax: +1-215-895-1934; Tel: +1-215-895-6446

^bDepartment of Applied Physics and Applied Mathematics, Columbia University, New York, NY 10027, USA

^cCenter for Functional Nanomaterials, Brookhaven National Laboratory, Upton, NY 11973, USA

^dCondensed Matter Physics and Materials Science Department, Brookhaven National Laboratory, Upton, NY 11973, USA

[†]Electronic supplementary information (ESI) available. See DOI: 10.1039/c7nr06721f

exfoliation of layered materials, while a gas-phase synthesis of GaN monolayers under graphene also exists.³⁰ Several of those studies, however, lacked focus on upscaling the methods and yielding 2D metal nitrides which could be easily implemented into devices, which is a major focus of this study.

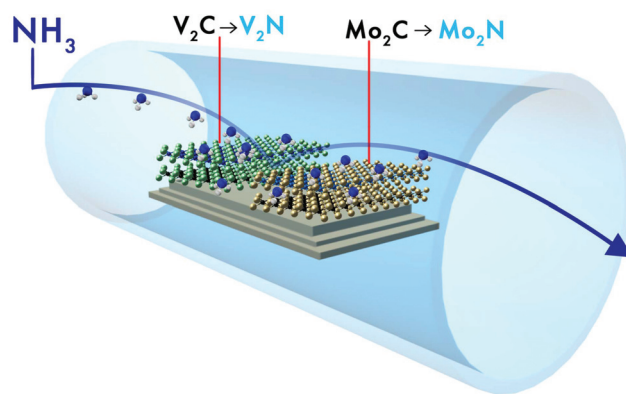
Exfoliation of MAX phases in aqueous hydrofluoric acid solutions, a common approach in synthesizing carbide MXenes, has not been successful in producing nitride MXenes. The instability of nitride MXenes in aqueous hydrofluoric acid, contrary to carbide MXenes, is related to how the formation energies of nitride MXenes (for example, $Ti_{n+1}N_n$) from their MAX phases (for example, $Ti_{n+1}AlN_n$) are greater than those of carbide MXenes ($Ti_{n+1}C_n$) from their MAX phase precursors ($Ti_{n+1}AlC_n$).³¹ It is also related to how cohesive energies of nitride MXenes are less than those of corresponding carbide MXenes.³¹ In other words, preparing nitride MXenes *via* etching in aqueous hydrofluoric acid has not been successful because it has not been possible to selectively etch the Al layer in the MAX phase precursor (e.g. Ti_4AlN_3) without dissolving or oxidizing the product.²⁸ While high-temperature chemical exfoliation methods for producing nitrides exist, high-yield gas-phase synthesis methods for producing 2D nitrides have not been focused on.

Heat treatment in ammonia (ammoniation) has been used on metal oxides to either N-dope them or transform oxides to 3D nitrides. Although ammoniation of 2D precursors such as GaSe to yield the 2D metal nitride GaN has been reported, the extent of the route of synthesizing other potential 2D metal nitrides *via* ammoniation has not been fully realized.³² TiO_2 can be N-doped by nitridation at 600 °C,^{33,34} and recently reported nitridation attempts of Ti_3C_2 have yielded only N-doped 2D carbides.³⁵ Ti_3C_2 was doped with nitrogen atoms by ammoniation at temperatures up to 700 °C in which N comprised up to 20.7 at% of the product.³⁵ It was only recently when synthesis of 2D metal nitrides *via* ammoniation was reported, including 2D MoN *via* the ammoniation of MoO_3 -coated NaCl.³⁶ In this study, we report the first transformation of Mo_2CT_x and V_2CT_x carbide MXenes into 2D metal nitrides *via* ammoniation at 600 °C. It is important to note that unlike previously reported 2D MoN and V_2N *via* salt-templated synthesis with 2D metal oxide precursors,³⁷ the 2D metal nitrides reported here, synthesized with carbide MXene precursors, have different crystal structures than those previously reported. Our results indicate that Mo_2N retains the MXene structure and V_2C transforms to a mixed layered structure of trigonal V_2N and cubic VN.

Experimental

Synthesis

The MXenes Mo_2CT_x and V_2CT_x were discovered recently and several works have since been published on their properties and novel synthesis methods.^{8,38–41} Experimental research on thermoelectric properties of Mo_2C has been studied.⁴² 2D carbide MXenes, produced after etching their precursor MAX phase, typically have multilayered structures.² Other bulk pre-



Scheme 1 Synthesis of 2D transition metal nitrides can be achieved by ammoniation of carbide MXenes (Mo_2CT_x and V_2CT_x) at elevated temperatures.

cursors for MXenes also exist.^{43,44} Multilayered powders can be delaminated into single- and few-layer flakes in solution using solvents and sonication, which can be collected *via* filtration to form flexible, freestanding films.² Films of delaminated Mo_2CT_x and V_2CT_x flakes with thicknesses ranging from 2 to 20 μm are described in the ESI.† To synthesize nitride MXenes, multilayer powders and delaminated films of Mo_2CT_x and V_2CT_x were treated at 600 °C for 1 h at a heating rate of 10 °C h^{-1} in an ammonia, NH_3 , atmosphere and cooled at the same rate. The ammonia flow rate through the reactor was approximately 300 $cm^3 min^{-1}$. During the reaction, nitridation occurs by the replacement of C atoms, in the Mo_2CT_x and V_2CT_x , with N atoms. A schematic of the process is shown in Scheme 1. The synthesis process is described in complete detail in the ESI.†

Results

Characterization

To determine whether nitridation occurred, as the first step, energy dispersive X-ray spectroscopy (EDX) in a scanning electron microscope (SEM) was performed to analyze the qualitative atomic compositions of the ammoniated products. SEM images of the delaminated MXene films after annealing in ammonia at 600 °C for 1 h are shown in Fig. 1a and b, for Mo_2N and V_2N , respectively. The structures of both samples suggest that the layered structure remains after ammoniation. Table 1 shows the atomic composition ratios detected by EDX, normalized to the metal M (Mo or V) = 2.00. As shown in Table 1, for Mo_2CT_x before treatment, the Mo:N:C ratio is 2.00:0.00:5.35, and after ammoniation at 600 °C, the nitrogen replacing carbon is evident by the change in ratio to 2.00:2.04:0.00. For V_2CT_x before treatment, the V:N:C ratio is 2.00:0.00:3.91, which changes to 2.00:2.46:0.58 after ammoniation at 600 °C. To optimize the ammoniation conditions, several temperatures were attempted. As evident in Table 1, as the temperature of ammoniation increases from 400 °C to 600 °C, the ratio of N to C greatly increases, with the amount of C decreasing most significantly at the 600 °C treat-

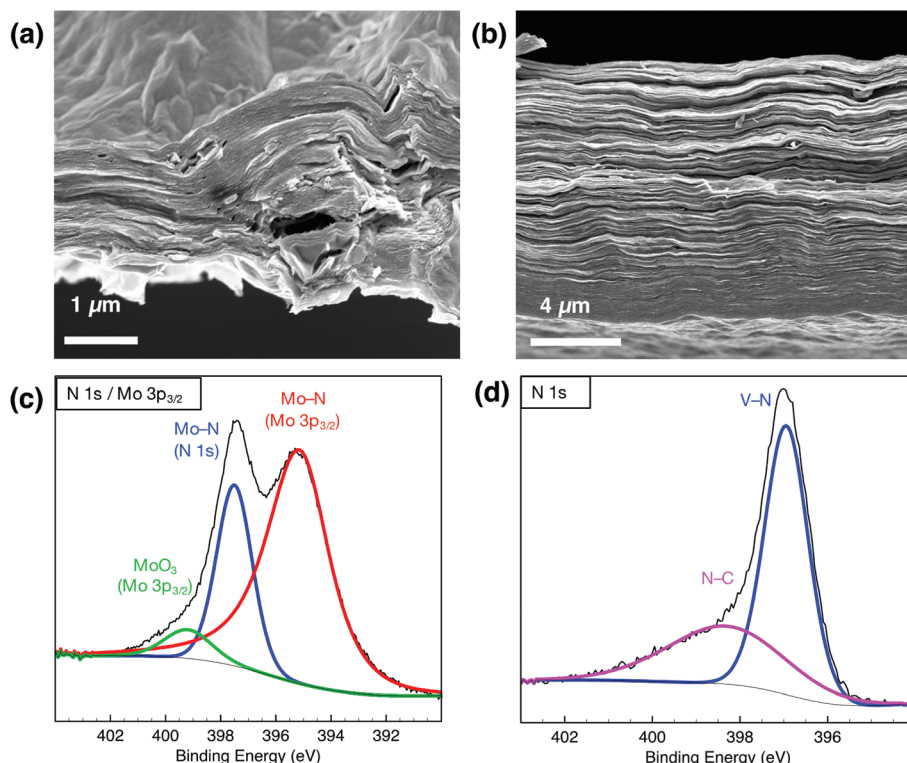


Fig. 1 The layered, 2D morphology of the delaminated films after ammoniation at 600 °C shown in the SEM images in (a) Mo₂N and (b) V₂N. Evidence for Mo–N bonding in Mo₂N is shown in the XPS spectrum in the N 1s/Mo 3p_{3/2} region in (c), while evidence of V–N bonding in V₂N is shown in (d).

Table 1 Summary of elemental analysis in EDX before and after ammoniation at various temperatures for 1 h, listed with standard error of the mean. Atomic ratios are normalized to Mo or V = 2.00 ± 0.00

	Mo	N	C	O	F
Mo ₂ C before	2.00 ± 0.00	—	5.35 ± 1.46	2.87 ± 0.18	0.32 ± 0.05
NH ₃ 600 °C	2.00 ± 0.00	2.04 ± 0.05	—	1.02 ± 0.05	—
NH ₃ 500 °C	2.00 ± 0.00	1.76 ± 0.18	3.03 ± 0.03	2.16 ± 0.08	—
NH ₃ 400 °C	2.00 ± 0.00	1.55 ± 0.22	2.13 ± 0.18	1.89 ± 0.13	—
	V	N	C	O	F
V ₂ C before	2.00 ± 0.00	—	3.91 ± 0.10	1.40 ± 0.01	1.30 ± 0.05
NH ₃ 600 °C	2.00 ± 0.00	2.46 ± 0.08	0.58 ± 0.02	—	—
NH ₃ 500 °C	2.00 ± 0.00	1.34 ± 0.27	1.19 ± 0.04	0.30 ± 0.10	0.16 ± 0.03
NH ₃ 400 °C	2.00 ± 0.00	0.86 ± 0.06	1.80 ± 0.06	1.43 ± 0.07	0.67 ± 0.02

ment. Since EDX does not quantify light elements (C and N) accurately, these results are presented to show not exact compositions of the products, but rather the trend of the composition of nitrogen and carbon in the products as the temperature is varied. Low- and high-magnification SEM images shown in Fig. S1 in the ESI† confirm that no separate oxide particles are present. Oxidation and the formation of oxides can occur when annealing MXenes in high temperature,² but the absence of oxide particles confirms that the material is stable against oxidation in ammonia, up to at least 600 °C.

To understand the nature of N detected in EDX and to confirm that nitridation occurred, X-ray photoelectron spectroscopy (XPS) measurements were performed on the Mo₂N

and V₂N films. XPS was performed to confirm that N was bonded to the metal atoms (Mo or V), and that the C–metal bonding was eliminated or diminished. High-resolution XPS spectra deconvolution for the N 1s region is shown for Mo₂N (Fig. 1c) and V₂N (Fig. 1d). Additional deconvolution for other regions are shown in Fig. S2 in the ESI.† The deconvolution for the various species and the elemental compositions extracted from the high-resolution spectra are tabulated in Tables S1 and S2 in the ESI† for Mo₂N and V₂N, respectively.

For Mo₂N, Fig. 1c shows the high-resolution spectrum of the N 1s/Mo 3p_{3/2} region. This region contains components from two different orbitals, therefore N 1s and Mo 3p components overlap. This region was fitted by components corres-

ponding to the following species: Mo–N (Mo 3p_{3/2}), Mo–N (N 1s) and MoO₃ (Mo 3p_{3/2}), confirming that N is bonded to Mo. Moreover, as indicated in Tables S1 and S2 in the ESI,[†] the C 1s regions of both nitrides show that there is either no or a very insignificant metal–C component for V₂N and Mo₂N, respectively, which should typically appear at ~282 eV,⁴⁵ confirming that N replaced C in these systems. The composition of all components fitted for this Mo₂N sample are tabulated in Table S1.[†] The fractions of N–Mo–T_x (Mo 3d) (21 at%), Mo–N (Mo 3p_{3/2}) (21 at%) and Mo–N (N 1s) (22 at%) are among the most prominent components. By taking the ratios of these two Mo components and one N component, the fraction of 2 : 1 ratio of Mo : N suggests a formula of Mo₂NT_x. This is, however, difficult to quantify, because a miniscule amount of the N–Mo–T_x (Mo 3d) component may also be attributed to C–Mo–T_x bonding. A C–Mo–T_x component was assigned in the C 1s spectrum (Fig. S2c[†]), indicating some non-nitridized carbide MXene particles are present (less than 1.0% of the area all fitted components in all regions, as shown in Table S1[†]). The T_x indicates the oxygen and hydroxyl terminating functional groups that are likely present on the surface, as suggested by the species detected in the O 1s region shown in Fig. S2b.[†]

For V₂N, Fig. 1d shows the high-resolution spectrum of the N 1s region. This region was fitted by components corres-

ponding to the species V–N and N–C. These two regions confirm that N is bonded to V in this system. The composition of all components fitted for this sample are tabulated in Table S2.[†] Based on these fractions of components in the V 2p and N 1s regions, if one assumes that all components in the V 2p region are a part of the nitride product, and the higher valency V⁴⁺ and V⁵⁺ components are oxygen-terminated –V–N–O_x components, then the 2 : 1 ratio of V : N may suggest a chemical formula of V₂NT_x. Similar to Mo₂NT_x, the T_x in this formula indicates the oxygen surface groups on the surface that were detected, shown in Fig. S2e.[†] Based on XPS, we can conclude that the C that was detected in EDX is not in the V₂N structure but rather from adventitious carbon.⁴⁶

After confirming that these products were nitrides, X-ray diffraction (XRD) was carried out on the ammoniated samples to determine whether the MXene structure was kept or new crystal phases were formed. As shown in the XRD patterns in Fig. 2a, after the ammoniation of Mo₂CT_x, the expected layered structure of a MXene is still maintained as evidenced by the (002) peak in the top pattern for Mo₂N, which represents the distance between MXene layers.² The (002) basal plane peak for Mo₂CT_x MXenes exists typically in the range of 2θ = 3 to 11°, depending on the number of intercalated water and other molecules.^{45,47} The (002) peak measured from Mo₂CT_x appears

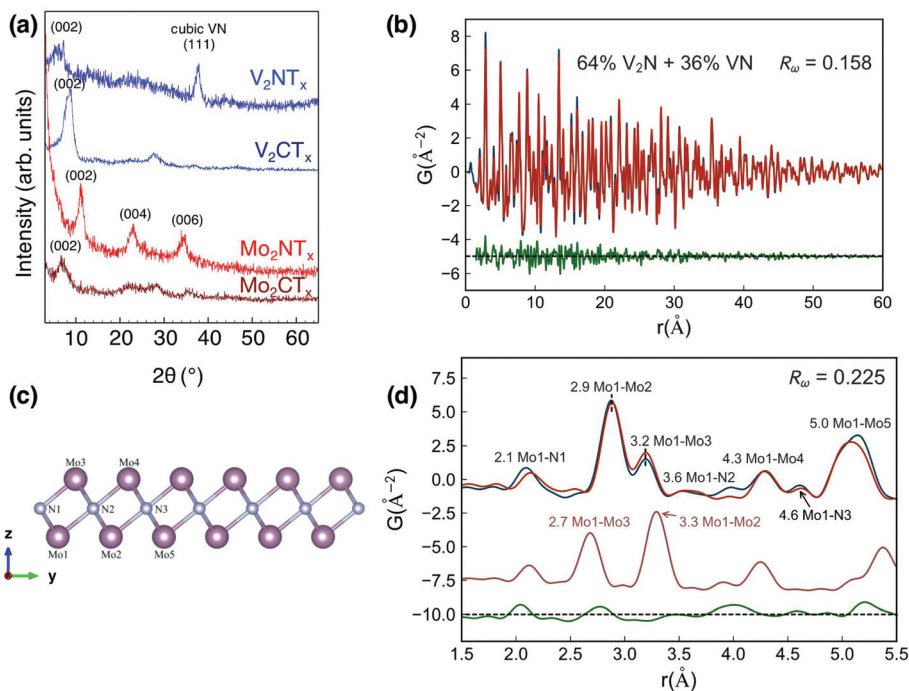


Fig. 2 (a) XRD patterns of Mo₂CT_x and V₂CT_x before and after (Mo₂NT_x and V₂NT_x) ammoniation at 600 °C for 1 h. After Mo₂CT_x was annealed at 600 °C it formed Mo₂NT_x and maintained its 2D MXene structure as evidenced by the presence of the (002) peak at 2θ = 11°. For V₂NT_x (top blue curve), a broad peak appears at 2θ = 7.0°, while the presence of a non-MXene nitride is evidenced by the peak at 37°. (b) X-ray pair distribution function (PDF) fit (red curve) of the 64% V₂N + 36% VN (mass ratio) mixed phase model to the measured data (blue) with difference curve offset below (green). R_w is the goodness of fit (a lower value corresponds to better fit). (c) Single slab model of Mo₂N MXene after structure refinement, projected along the x-axis. (d) PDF fit (top red curve) of the Mo₂N single slab model after structure refinement to the measured data (top blue) with a difference curve offset (bottom green). Simulated PDF of the initial Mo₂N MXene single slab model (having the same atomic positions as the precursor Mo₂C MXene structural model) without structure refinement (middle brown) is shown in the offset below the measured data (top blue).

at about 7° , due to the expansion of the layers after the intercalation of water and the delaminating solvent tetrabutylammonium hydroxide (TBAOH), as described in the ESI.†⁴⁵ After ammoniation at 600°C , the (002) peak shifts to $\sim 11.4^\circ$, corresponding to an average interlayer distance of 7.8 \AA . This value is in the range of what is predicted for the functionalized M_2XT_x MXenes with no intercalated molecules (M represents a transition metal).⁴⁷ As shown in Fig. S3a in the ESI,† the Mo_2XT_x (X referring to either C or N) MXene (002) peak shifts to about $2\theta = 9^\circ$ after the sample was ammoniated at 400°C and 500°C . It is only after the sample was ammoniated at 600°C that the peak shifts to about 11° , indicating that the spacing between the 2D layers is smaller after the higher temperature processing. We attribute this contraction to the complete removal of intercalated molecules and possibly some of the functional groups such as $-\text{F}$ and of confined water.⁴⁷ There are other peaks at larger 2θ observed for the as-synthesized and ammoniated at 600°C Mo_2CT_x that all correspond to the (00*l*) basal plane peaks, indicating that the layer stacking is somewhat regular. In the case of ammoniation at 600°C , two peaks are located at ~ 23 and 34° corresponding to the (004) and (006) peaks of MXene. This suggests that the resulting phase is Mo_2NT_x , as these peaks correspond to higher-order ordering of MXene layers. The other possible phase to form is hexagonal MoN (*h*-MoN). However, *h*-MoN XRD peaks do not match any peaks of the collected pattern. The first and major peak of *h*-MoN at 36° corresponds to its (200) planes,³⁶ where there is no peak observed in the Mo_2NT_x pattern (Fig. 2a).

The (002) peak of V_2CT_x consists of a doublet in the range of about $2\theta = 8\text{--}9^\circ$, indicating intercalated water and TBAOH molecules and functional groups. There are higher order (00*l*) peaks at lower intensities, indicating the regular periodic stacking of MXene layers over an extended range. After ammoniation, a broad peak appears around 7.0° , which can be related to the (002) peak of a MXene structure, and perhaps indicating that the interlayer spacing is increased after ammoniation. Additionally, ammoniation results in the appearance of a new peak at 37° , which can be assigned to the (111) peak of cubic VN.^{48,49}

To obtain a more quantitative determination of the atomic structure and morphology of the nitride flakes, X-ray pair distribution function (PDF) analysis was conducted on the Mo_2NT_x and V_2NT_x .^{50,51} The samples analyzed were prepared by ammoniating multilayered Mo_2CT_x and V_2CT_x , respectively. The data acquisition, data reduction, and structural modeling are described in greater detail in the ESI.†^{52–57}

We first discuss the structure of the vanadium compound. The measured PDF data have sharp peaks over a wide range of r (blue curve in Fig. 2b) indicating that the nitride products have relatively well-ordered structures and are of sufficient quality to refine quantitative structures. The data in the high- r region (up to $r = 60\text{ \AA}$) were well fit to a trigonal V_2N structure (space group $P\bar{3}1m$) (Fig. S4†) with atoms sitting at the following special positions: V ($x, 0, z$), N1 ($1/3, 2/3, 1/2$), and N2 ($0, 0, 0$).⁵⁸ The fit was satisfied in the high- r region; however, in the low- r region, there was a significant difference

between the measured data and model (green curves offset below in Fig. S5a and S5b†) suggesting that this model did not explain all the features observed in the data. We therefore added a second phase, cubic VN (space group $Fm\bar{3}m$) (Fig. S6†) with a finite size, to the modeling with atoms sitting at the following special positions: V ($0, 0, 0$) and N ($1/2, 1/2, 1/2$).⁵⁹ The fit was improved with the refined mass fraction of 36% and size of around 2 nm for the VN phase. The PDF fit of this mixed phase model is shown in Fig. 2b and the refined structural parameters are shown in Table 2.

The structure of Mo_2N , on the other hand, can be described as a distorted MXene structure, created by cutting a single slab of atoms from its respective crystal structure, shown in Fig. 2c.⁶⁰ We used the Debye scattering equation to calculate the PDF of a single slab using the DiffPy-CMI program.^{57,61} It is clear from the PDF of Mo_2N in Fig. 2d (blue curve), that the local structure has lower symmetry than the V_2N , for example the PDF peak centered around $r = 3\text{ \AA}$, which is the Mo–Mo nearest neighbor distance, is split into two. Such a distinct set of Mo–Mo distances was seen in the hexagonal carbide Mo_2C MXene precursor structure. However, the simulated PDF of the Mo_2C structural model (brown curve in Fig. 2d) did not fit the measured data (blue curve in Fig. 2d) well. We were able to fit the measured data well over the low- r range by staying in the same Wyckoff sites, but by squeezing a single slab of Mo_2N along in-plane dimensions and extending along the out-of-plane dimension (z -direction). This caused the distance between nearest Mo atoms on the same z -coordinate plane (*e.g.* Mo1–Mo2 in Fig. 2c) to decrease from 3.3 to 2.9 \AA , while the distance between nearest Mo atoms separated along the z -direction (still within a single slab, *e.g.* Mo1–Mo3 in Fig. 2c) to increase from 2.7 to 3.2 \AA . The distortion in the Mo_2N structure is the opposite from that in the Mo_2C . In the latter, out-of-plane Mo–Mo distances are shorter than the in-plane Mo–Mo distances. This has implications for the electronic structure and electrical properties that require further study. The refined structural parameters are shown in Table 3.

Table 2 Structure refinement result of the vanadium product, fit to trigonal V_2N and cubic VN mixed phase model. Q_{damp} and Q_{broad} parameters were refined in a fit to a standard calibration sample (see ESI for details) and then fixed to 0.0369 \AA^{-1} and 0.0131 \AA^{-1} , respectively. For the VN phase, its lattice parameters were constrained as $a = c$ due to cubic symmetry, and its isotropic atomic displacement parameters $U_{\text{iso}}(\text{V})$ and $U_{\text{iso}}(\text{N})$ were constrained in the same way as those in the V_2N phase. Spdiameter is the particle diameter parameter for PDF shape damping function

Fitting range (\AA)	1.5 to 60	
R_w	0.158	
Phase	V_2N	VN
Mass ratio	64%	36%
a (\AA)	5.0415	4.1267
c (\AA)	4.3724	4.1267
x (V)	0.6716	—
z (V)	0.7509	—
$U_{\text{iso}}(\text{V})$ (\AA^2)	0.0032	0.0032
$U_{\text{iso}}(\text{N})$ (\AA^2)	0.0118	0.0118
Spdiameter (\AA)	—	21.3486

Table 3 The structure refinement result of Mo_2N . The Mo_2N single slab model was created by cutting a single slab of atoms from its respective bulk crystal structure. The atoms are sitting at the following special positions: Mo1 at (1/3, 2/3, z), Mo2 at (0, 0, z), and N (1/3, 2/3, z). Q_{damp} and Q_{broad} parameters were refined in a fit to a standard calibration sample (see ESI for details) and then fixed to 0.0369 \AA^{-1} and 0.0131 \AA^{-1} , respectively

Fitting range (\AA)	1.5 to 5.5
R_w	0.225
a (\AA)	2.8850
z (Mo1)	0.4348
z (Mo2)	0.0713
z (N)	0.0019
$U_{\text{iso}}(\text{Mo})$ (\AA^2)	0.0048
$U_{\text{iso}}(\text{N})$ (\AA^2)	0.0021

To corroborate conclusions based on the X-ray PDF, high-resolution transmission electron microscopy (TEM) was then used. TEM images were acquired on a JEOL2100F high resolution TEM, at accelerating voltage 200 kV. For the TEM images and selected area electron diffraction (SAED) patterns in Fig. 3, as-produced multilayered Mo_2NT_x and V_2NT_x (ammoniated Mo_2CT_x and V_2CT_x at $600 \text{ }^\circ\text{C}$) were examined instead of delaminated films to minimize the effects of post-treatment. Because these are multilayered powders, they are relatively thicker than would be delaminated single-layer sheets of Mo_2NT_x and V_2NT_x . As shown in the inset in Fig. 3a, the SAED for the Mo_2NT_x particle is hexagonal, similar to the pattern of its carbide MXene precursor's basal plane (space group $P6_3/mmc$). The distance between the nearest spots in SAED is 4.16 nm^{-1} . It does not, therefore, correspond to the distance expected for 2D h - MoN for the (001) plane's pattern (5.18 nm^{-1}),³⁶ but rather to a distorted $P6_3/mmc$ structure, which is in agreement with the XRD and X-ray PDF results. For the V_2NT_x SAED in Fig. 3b, the hexagonal pattern shown could be attributed to the (001) plane of trigonal V_2N or the (111) plane of the cubic VN present in the sample, as determined by the X-ray PDF and XRD results.

Electrical conductivity characterization

After confirming the crystal structure and composition of these two transition metal nitrides Mo_2NT_x and V_2NT_x , their electronic properties were measured. Electronic properties of Mo_2CT_x and V_2CT_x before and after heat treatments were studied in a Quantum Design EverCool II Physical Property Measurement System (PPMS). A free-standing film with a thickness $\sim 20 \text{ }\mu\text{m}$ of each sample was cut to a $5 \times 5 \text{ mm}$ square, and silver wires were attached onto the film in a 4-point probe geometry using adhesive silver paint. In-plane temperature-dependent resistivity was recorded from room temperature (300 K) down to 10 K in a low pressure helium environment ($\sim 20 \text{ Torr}$).

Shown in Fig. 4a are temperature-dependent resistivity of pristine Mo_2CT_x and its heat-treated and gas-treated derivatives. The room-temperature resistivity of pristine Mo_2CT_x , and Mo_2NT_x are 3.6×10^{-1} and $4.8 \times 10^{-4} \text{ }\Omega \text{ cm}$, respectively. The resistivity of the pristine Mo_2CT_x is similar to that reported earlier.⁴⁵ Note that the pristine sample in this work refers to the as-synthesized film annealed in vacuum at $150 \text{ }^\circ\text{C}$ for 3 h to remove adsorbed and/or intercalated molecules. The resistivity of pristine Mo_2CT_x increases with decreasing temperature down to 40 K (semiconductor-like behavior), after which the resistivity rises more sharply. This change in conduction mechanism in the low temperature regime was also observed in the previous report on Mo_2CT_x , which was attributed to the variable range hopping (VRH) mechanism.⁴⁵ In contrast, the resistivity of Mo_2NT_x first decreases when the temperature is decreased from 300 K to 100 K, and remains roughly constant down to 10 K. The drastic changes in both the absolute value of resistivity and the shape of resistivity *versus* temperature plot suggests changes in the conduction mechanism and/or electronic structure caused by ammoniation. Metallic conductivity observed for the Mo_2NT_x is consistent with that of bulk non-MXene Mo_2N .⁶² For comparison, the precursor MXene Mo_2CT_x film was treated at $600 \text{ }^\circ\text{C}$ with the same conditions

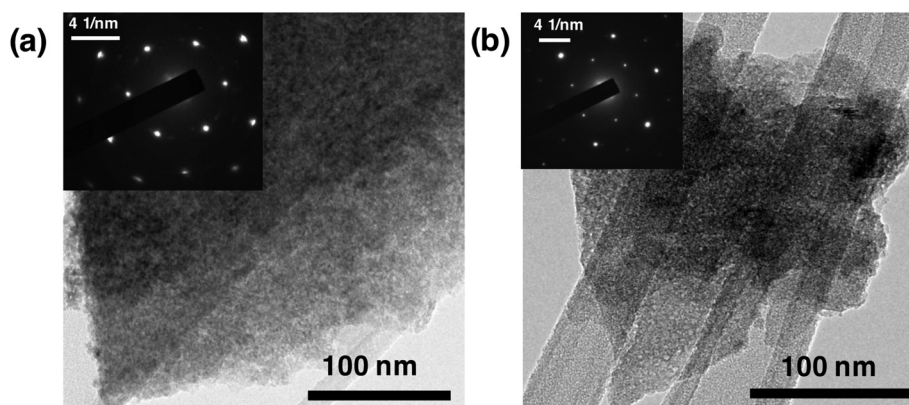


Fig. 3 (a) TEM micrograph of Mo_2NT_x synthesized by the ammoniation of multilayered Mo_2CT_x at $600 \text{ }^\circ\text{C}$. (b) TEM micrograph of V_2NT_x synthesized by the ammoniation of multilayered V_2CT_x at $600 \text{ }^\circ\text{C}$. The insets show the selected-area diffraction patterns in these regions. Each shows hexagonal basal plane symmetry. In the case of (a), this could be attributed to the (001) plane of the MXene structure. In the case of (b), this could be attributed to the (001) plane of trigonal V_2N , or (111) plane of cubic VN.

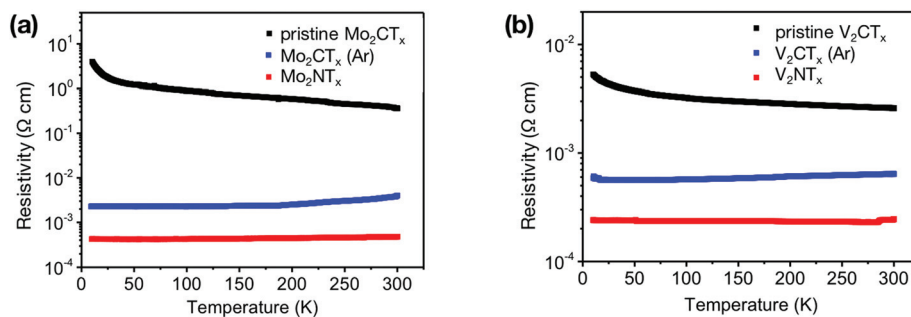


Fig. 4 Temperature-dependent resistivity of (a) Mo_2NT_x and (b) V_2NT_x . The various curves in each correspond to the pristine carbide MXene precursor (Mo_2CT_x and V_2CT_x) (black curves), the MXene after treatment in Ar at 600 °C (Mo_2CT_x (Ar) and V_2CT_x (Ar)) (blue curves), and the nitride Mo_2NT_x and V_2NT_x synthesized by treating their respective carbide MXene precursors in NH_3 at 600 °C (red curves). The behavior of the dependence of resistivity on temperature changes as a result of the heat treatments to a more metallic behavior. The decrease in resistivity (increase in conductivity) is greatest after the pristine MXenes are treated in NH_3 .

except that flowing Ar gas was used to create an inert environment instead of NH_3 , to determine if the change in resistivity was dependent on heat-treatment regardless of the atmosphere, the atmosphere, or a combination of both. The resistivity of the Ar-treated Mo_2CT_x (Mo_2CT_x (Ar)) was measured to be $4.0 \times 10^{-3} \Omega \text{ cm}$ and similar to Mo_2N , the Ar-treated Mo_2CT_x (Mo_2CT_x (Ar)) also shows decreasing resistivity with decreasing temperature. A clear metallic behavior of Mo_2CT_x (Ar) and Mo_2NT_x can be seen in Fig. S11.† However, the room-temperature resistivity of Mo_2CT_x (Ar) is an order of magnitude higher than that of Mo_2NT_x . Hence, we conclude that the change in electronic conduction behavior of Mo_2CT_x MXene after ammoniation stems from synergistic effects of the transformation from carbide to nitride as well as the removal of intercalated molecules and surface functionalities at high temperature.

For V_2CT_x MXene, the room-temperature resistivity of pristine V_2CT_x , V_2CT_x (Ar), and V_2NT_x are 2.6×10^{-3} , 6.4×10^{-4} , and $2.4 \times 10^{-4} \Omega \text{ cm}$, respectively. Temperature-dependent resistivity of V_2CT_x MXene and its heat-treated derivative are presented in Fig. 4b. The pristine V_2CT_x shows semiconductor-like behavior where the resistivity increases from $2.6 \times 10^{-3} \Omega \text{ cm}$ at room temperature to $5.3 \times 10^{-3} \Omega \text{ cm}$ at 10 K. Similar to Mo_2CT_x , ammoniation and heat treatment of V_2CT_x in an inert environment lead to lower resistivity and change from semiconductor-like to metallic behavior. This change in behavior is consistent with first principle calculations that OH- and F-terminated V_2CT_x are small-bandgap semiconductor, while non-terminated monolayer V_2CT_x and V_2NT_x are metallic.^{63,64}

Conclusions

In summary, with different analytical techniques including SEM, EDX, XRD, and X-ray PDF we present evidence of the first transformation of MXene carbides (Mo_2CT_x and V_2CT_x) to 2D nitrides by ammoniation. This was achieved by ammoniating Mo_2CT_x and V_2CT_x MXenes at elevated temperatures (up to 600 °C for 1 h). Nitridation lead to the replacement of C atoms

with N atoms from the ammonia (NH_3) and transformed the carbide MXenes into nitrides. Based on our characterization results, ammoniation of Mo_2CT_x at 600 °C for 1 h yields Mo_2NT_x with a layered MXene structure, where compared to the MXene carbide, in-plane molybdenum bonds are shorter than their out of plane bonds. However, ammoniation of V_2CT_x at the same conditions yields a mixed phase of trigonal V_2N and cubic VN. Temperature-dependent resistivity determined that compared to pristine Mo_2CT_x and V_2CT_x , heat treating the samples at 600 °C for 1 h in Ar and NH_3 increased the electrical conductivity by orders of magnitude, with ammoniation resulting in the greatest increase in electrical conductivity. These heat treatments also changed the temperature dependence of resistivity.

Conflicts of interest

There are no conflicts of interest to declare.

Acknowledgements

We thank Christine Hatter for conducting preliminary TEM measurements, Patrick Walsh for help with MXene synthesis, as well as Saleesha Sin for designing the schematic of ammoniation (all Drexel University). This work was supported by the U.S. National Science Foundation under grant number DMR-1310245. This research used JEOL2100F HRTEM of the Center for Functional Nanomaterials, which is a U.S. DOE Office of Science Facility, at Brookhaven National Laboratory under Contract No. DE-SC0012704. X-ray PDF measurements were conducted on beamline 28-ID-2 of the National Synchrotron Light Source II, a U.S. Department of Energy (DOE) Office of Science User Facility operated for the DOE Office of Science by Brookhaven National Laboratory under Contract No. DE-SC0012704. Long Yang and Simon Billinge acknowledge financial support from the NSF MRSEC program through Columbia in the Center for Precision Assembly of

Superstratic and Superatomic Solids (DMR-1420634). We also acknowledge support from the Drexel Areas of Research Excellence (DARE) initiative.

Notes and references

- M. Naguib, M. Kurtoglu, V. Presser, J. Lu, J. Niu, M. Heon, L. Hultman, Y. Gogotsi and M. W. Barsoum, *Adv. Mater.*, 2011, **23**, 4248–4253.
- B. Anasori, M. R. Lukatskaya and Y. Gogotsi, *Nat. Rev. Mater.*, 2017, **2**, 16098.
- P. Eklund, J. Rosen and P. O. Å. Persson, *J. Phys. D: Appl. Phys.*, 2017, **50**, 113001.
- M. Khazaei, A. Ranjbar, M. Arai, T. Sasaki and S. Yunoki, *J. Mater. Chem. C*, 2017, **5**, 2488–2503.
- V. M. H. Ng, H. Huang, K. Zhou, P. S. Lee, W. Que, J. Z. Xu and L. B. Kong, *J. Mater. Chem. A*, 2017, **5**, 3039–3068.
- M. Ghidui, M. R. Lukatskaya, M.-Q. Zhao, Y. Gogotsi and M. W. Barsoum, *Nature*, 2014, **516**, 78–81.
- M. R. Lukatskaya, O. Mashtalir, C. E. Ren, Y. Dall'Agnese, P. Rozier, P. L. Taberna, M. Naguib, P. Simon, M. W. Barsoum and Y. Gogotsi, *Science*, 2013, **341**, 1502–1505.
- M. Naguib, J. Halim, J. Lu, K. M. Cook, L. Hultman, Y. Gogotsi and M. W. Barsoum, *J. Am. Chem. Soc.*, 2013, **135**, 15966–15969.
- M.-Q. Zhao, C. E. Ren, Z. Ling, M. R. Lukatskaya, C. Zhang, K. L. Van Aken, M. W. Barsoum and Y. Gogotsi, *Adv. Mater.*, 2015, **27**, 339–345.
- F. Shahzad, M. Alhabeab, C. B. Hatter, B. Anasori, S. Man Hong, C. M. Koo and Y. Gogotsi, *Science*, 2016, **353**, 1137–1140.
- J. Liu, H.-B. Zhang, R. Sun, Y. Liu, Z. Liu, A. Zhou and Z.-Z. Yu, *Adv. Mater.*, 2017, 1702367, DOI: 10.1002/adma.201702367.
- K. Rasool, M. Helal, A. Ali, C. E. Ren, Y. Gogotsi and K. A. Mahmoud, *ACS Nano*, 2016, **10**, 3674–3684.
- C. E. Ren, K. B. Hatzell, M. Alhabeab, Z. Ling, K. A. Mahmoud and Y. Gogotsi, *J. Phys. Chem. Lett.*, 2015, **6**, 4026–4031.
- J. Halim, M. R. Lukatskaya, K. M. Cook, J. Lu, C. R. Smith, L.-Å. Näslund, S. J. May, L. Hultman, Y. Gogotsi, P. Eklund and M. W. Barsoum, *Chem. Mater.*, 2014, **26**, 2374–2381.
- A. D. Dillon, M. J. Ghidui, A. L. Krick, J. Griggs, S. J. May, Y. Gogotsi, M. W. Barsoum and A. T. Fafarman, *Adv. Funct. Mater.*, 2016, **26**, 4162–4168.
- K. Hantanasirisakul, M. Q. Zhao, P. Urbankowski, J. Halim, B. Anasori, S. Kota, C. E. Ren, M. W. Barsoum and Y. Gogotsi, *Adv. Electron. Mater.*, 2016, **2**, 1600050.
- B. Xu, M. Zhu, W. Zhang, X. Zhen, Z. Pei, Q. Xue, C. Zhi and P. Shi, *Adv. Mater.*, 2016, **28**, 3333–3339.
- C. J. Zhang, B. Anasori, A. Seral-Ascaso, S. H. Park, N. McEvoy, A. Shmeliov, G. S. Duesberg, J. N. Coleman, Y. Gogotsi and V. Nicolosi, *Adv. Mater.*, 2017, **29**(36), 1702678.
- M. Zhu, Y. Huang, Q. Deng, J. Zhou, Z. Pei, Q. Xue, Y. Huang, Z. Wang, H. Li, Q. Huang and C. Zhi, *Adv. Energy Mater.*, 2016, **6**, 1600969.
- H. Fashandi, M. Dahlgqvist, J. Lu, J. Palisaitis, S. I. Simak, I. A. Abrikosov, J. Rosen, L. Hultman, M. Andersson, A. Lloyd Spetz and P. Eklund, *Nat. Mater.*, 2017, **16**, 814–818.
- Q. Tao, M. Dahlgqvist, J. Lu, S. Kota, R. Meshkian, J. Halim, J. Palisaitis, L. Hultman, M. W. Barsoum and P. O. Persson, *Nat. Commun.*, 2017, **8**, 14949.
- G. V. Naik, J. L. Schroeder, X. Ni, A. V. Kildishev, T. D. Sands and A. Boltasseva, *Opt. Mater. Express*, 2012, **2**, 478–489.
- B. Soundiraraju and B. K. George, *ACS Nano*, 2017, **11**, 8892–8900.
- A. Morel, Y. Borjon-Piron, R. L. Porto, T. Brousse and D. Bélanger, *J. Electrochem. Soc.*, 2016, **163**, A1077–A1082.
- Y. Zhong, X. Xia, F. Shi, J. Zhan, J. Tu and H. J. Fan, *Adv. Sci.*, 2016, **3**, 1500286.
- J. Xie, S. Li, X. Zhang, J. Zhang, R. Wang, H. Zhang, B. Pan and Y. Xie, *Chem. Sci.*, 2014, **5**, 4615–4620.
- M. W. Barsoum, in *MAX Phases*, Wiley-VCH Verlag GmbH & Co. KGaA, 2013, ch. 1, pp. 1–12, DOI: 10.1002/9783527654581.
- P. Urbankowski, B. Anasori, T. Makaryan, D. Er, S. Kota, P. L. Walsh, M. Zhao, V. B. Shenoy, M. W. Barsoum and Y. Gogotsi, *Nanoscale*, 2016, **8**, 11385–11391.
- Q. Ye, P. Xiao, W. Liu, K. Chen, T. Chen, J. Xue, S. Du and Q. Huang, *RSC Adv.*, 2015, **5**, 70339–70344.
- Z. Y. Al Balushi, K. Wang, R. K. Ghosh, R. A. Vilá, S. M. Eichfeld, J. D. Caldwell, X. Qin, Y.-C. Lin, P. A. DeSario and G. Stone, *Nat. Mater.*, 2016, **15**, 1166–1171.
- I. R. Shein and A. L. Ivanovskii, *Comput. Mater. Sci.*, 2012, **65**, 104–114.
- M. Sreedhara, K. Vasu and C. Rao, *Z. Anorg. Allg. Chem.*, 2014, **640**, 2737–2741.
- S. Sakthivel and H. Kisch, *ChemPhysChem*, 2003, **4**, 487–490.
- G. Liu, L. Wang, C. Sun, X. Yan, X. Wang, Z. Chen, S. C. Smith, H.-M. Cheng and G. Q. Lu, *Chem. Mater.*, 2009, **21**, 1266–1274.
- Y. Wen, T. E. Rufford, X. Chen, N. Li, M. Lyu, L. Dai and L. Wang, *Nano Energy*, 2017, **38**, 368–376.
- X. Xiao, H. Yu, H. Jin, M. Wu, Y. Fang, J. Sun, Z. Hu, T. Li, J. Wu, L. Huang, Y. Gogotsi and J. Zhou, *ACS Nano*, 2017, **11**, 2180–2186.
- X. Xiao, H. Song, S. Lin, Y. Zhou, X. Zhan, Z. Hu, Q. Zhang, J. Sun, B. Yang, T. Li, L. Jiao, J. Zhou, J. Tang and Y. Gogotsi, *Nat. Commun.*, 2016, **7**, 11296.
- M. Khazaei, M. Arai, T. Sasaki, M. Estili and Y. Sakka, *Phys. Chem. Chem. Phys.*, 2014, **16**, 7841–7849.
- R. Meshkian, L.-Å. Näslund, J. Halim, J. Lu, M. W. Barsoum and J. Rosen, *Scr. Mater.*, 2015, **108**, 147–150.

- 40 C. Xu, L. Wang, Z. Liu, L. Chen, J. Guo, N. Kang, X.-L. Ma, H.-M. Cheng and W. Ren, *Nat. Mater.*, 2015, **14**, 1135–1141.
- 41 D. Geng, X. Zhao, Z. Chen, W. Sun, W. Fu, J. Chen, W. Liu, W. Zhou and K. P. Loh, *Adv. Mater.*, 2017, **29**(35), 1700072.
- 42 H. Kim, B. Anasori, Y. Gogotsi and H. N. Alshareef, *Chem. Mater.*, 2017, **29**, 6472–6479.
- 43 J. Zhou, X. Zha, X. Zhou, F. Chen, G. Gao, S. Wang, C. Shen, T. Chen, C. Zhi, P. Eklund, S. Du, J. Xue, W. Shi, Z. Chai and Q. Huang, *ACS Nano*, 2017, **11**, 3841–3850.
- 44 J. Zhou, X. Zha, F. Y. Chen, Q. Ye, P. Eklund, S. Du and Q. Huang, *Angew. Chem.*, 2016, **128**, 5092–5097.
- 45 J. Halim, S. Kota, M. R. Lukatskaya, M. Naguib, M. Q. Zhao, E. J. Moon, J. Pitock, J. Nanda, S. J. May and Y. Gogotsi, *Adv. Funct. Mater.*, 2016, **26**, 3118–3127.
- 46 J. Landoulsi, M. J. Genet, S. Fleith, Y. Toure, I. Liascukiene, C. Methivier and P. G. Rouxhet, *Appl. Surf. Sci.*, 2016, **383**, 71–83.
- 47 K. D. Fredrickson, B. Anasori, Z. W. Seh, Y. Gogotsi and A. Vojvodic, *J. Phys. Chem. C*, 2016, **120**, 28432–28440.
- 48 T. Huang, S. Mao, G. Zhou, Z. Wen, X. Huang, S. Ci and J. Chen, *Nanoscale*, 2014, **6**, 9608–9613.
- 49 X. Zhou, H. Chen, D. Shu, C. He and J. Nan, *J. Phys. Chem. Solids*, 2009, **70**, 495–500.
- 50 T. Egami and S. J. Billinge, *Underneath the Bragg peaks: structural analysis of complex materials*, Newnes, 2nd edn, 2012.
- 51 C. Shi, M. Beidaghi, M. Naguib, O. Mashtalir, Y. Gogotsi and S. J. Billinge, *Phys. Rev. Lett.*, 2014, **112**, 125501.
- 52 P. J. Chupas, X. Qiu, J. C. Hanson, P. L. Lee, C. P. Grey and S. J. Billinge, *J. Appl. Crystallogr.*, 2003, **36**, 1342–1347.
- 53 P. Juhás, T. Davis, C. L. Farrow and S. J. Billinge, *J. Appl. Crystallogr.*, 2013, **46**, 560–566.
- 54 X. Yang, P. Juhas, C. L. Farrow and S. J. Billinge, *arXiv preprint arXiv:1402.3163*, 2014.
- 55 T. Proffen and S. Billinge, *J. Appl. Crystallogr.*, 1999, **32**, 572–575.
- 56 C. Farrow, P. Juhas, J. Liu, D. Bryndin, E. Božin, J. Bloch, T. Proffen and S. Billinge, *J. Phys.: Condens. Matter*, 2007, **19**, 335219.
- 57 P. Juhás, C. L. Farrow, X. Yang, K. R. Knox and S. J. Billinge, *Acta Crystallogr., Sect. A: Found. Adv.*, 2015, **71**, 562–568.
- 58 A. N. Christensen and B. Lebech, *Acta Crystallogr., Sect. B: Struct. Crystallogr. Cryst. Chem.*, 1979, **35**, 2677–2678.
- 59 S. Hosoya, T. Yamagishi and M. Tokonami, *J. Phys. Soc. Jpn.*, 1968, **24**, 363–367.
- 60 K. Fukuda, M. Morita, S. Toyoda, A. Nakata, K. Tanaka, Y. Uchimoto and E. Matsubara, *Chem. Mater.*, 2016, **28**, 8899–8904.
- 61 P. Debye, *Ann. Phys.*, 1915, **351**, 809–823.
- 62 V. Anitha, S. Major, D. Chandrashekharam and M. Bhatnagar, *Surf. Coat. Technol.*, 1996, **79**, 50–54.
- 63 J. Hu, B. Xu, C. Ouyang, S. A. Yang and Y. Yao, *J. Phys. Chem. C*, 2014, **118**, 24274–24281.
- 64 G. Gao, G. Ding, J. Li, K. Yao, M. Wu and M. Qian, *Nanoscale*, 2016, **8**, 8986–8994.